High resolution magnetic microscopy based on semi-encapsulated graphene Hall sensors

Penglei Li[1], David Collomb[1], Zhen Jieh Lim[1], Sara Dale[1], Philippa Shepley[2], Gavin Burnell[2], and Simon J. Bending[1a)]

AFFILIATIONS

[1]Department of Physics, University of Bath, Claverton Down, Bath, BA2 7AY, UK

[2]School of Physics and Astronomy, University of Leeds, Leeds, LS2 9JT, UK

[a)]Author to whom correspondence should be addressed: s.bending@bath.ac.uk

ABSTRACT

The realisation of quantitative, non-invasive sensors for ambient magnetic imaging with high spatial and magnetic field resolution remains a major challenge. To address this we have developed a relatively simple process to fabricate semi-encapsulated graphene/hBN Hall sensors assembled by dry transfer onto pre-patterned gold contacts. 1μm-sized Hall cross sensors at a drive current of 0.5μA exhibit excellent room temperature sensitivity, S_I ~ 700V/AT, and good minimum detectable fields, B_{min} = 0.54G/Hz$^{0.5}$ at a measurement frequency of 1kHz, with considerable scope for further optimisation of these parameters. We illustrate their application in an imaging study of labyrinth magnetic domains in a ferrimagnetic yttrium iron garnet film.

MAIN TEXT

There is a growing demand for ambient magnetic imaging tools with higher spatial resolution and lower minimum detectable fields, driven for example by rapid increases in the density of magnetic data storage media as well as applications for susceptometry in non-destructive evaluation (NDE). A typical requirement might be to image domain walls in a ferromagnetic thin film which needs a spatial resolution of a few tens of nanometres and a field resolution of several tens of milliTeslas. The imaging technique of choice in the data storage industry remains magnetic force microscopy (MFM) [1,2] which is capable of high spatial (~10-50nm) and temporal resolutions and reasonable minimum detectable fields of B_{min} ~ 200nT/Hz$^{0.5}$ in ac imaging modes. However, the ferromagnetic MFM tip is invasive and its micromagnetic state is rarely known with any confidence, making the extraction of quantitative information challenging. Several other ambient scanning probe techniques have been developed in recent years to address these issues including scanning magnetoresistive (SMR) sensors [3], scanning Hall probe microscopy (SHPM) [4,5] and diamond Nitrogen vacancy (NV) microscopy [6].

SMR imaging using commercial hard drive tunnel magnetoresistance (TMR) read heads has achieved ~50nm spatial resolution and typical minimum detectable fields, B_{min} ~ 10nT/Hz$^{0.5}$ while Bi-based scanning Hall probes have demonstrated ~50nm spatial resolution and B_{min} ~ 80μT/Hz$^{0.5}$. Recent developments in NV imaging look very promising and combine high spatial resolution (~15-25nm) with excellent minimum detectable fields (B_{min} ~ 100nT/Hz$^{0.5}$), albeit with relatively low temporal resolution. However, these systems are complex, combining optical spectroscopy, microwave excitation and scanning probe techniques, and variable temperature set-ups seem unlikely to become turnkey products in the near future. In contrast SHPM systems are much more compact and relatively straightforward to use, they are also virtually *noninvasive* and generate *quantitative* maps of the out-of-plane component of magnetic induction at a sample surface, allowing their ready adoption in a wide range of applications [7].

The spatial resolution of state-of-the-art SHPM now quite closely rivals MFM, and functional 50nm semimetal Bi Hall probes have been demonstrated, patterned with a Ga^+ focused ion beam in a polycrystalline thin film [8]. However, such sensors exhibit an inevitable resolution trade-off and the minimum detectable field normally scales *inversely* with sensor size. The fundamental limit on scanning Hall sensors at measurement frequencies above the 1/f noise corner is set by Johnson noise arising in the voltage leads. In this limit the minimum detectable field is given by

$$B_{min}^{J} = \frac{1}{I_H}\sqrt{\frac{n_{2D}}{\mu}}\sqrt{\frac{4lek_BT\Delta f}{w}}, \qquad (1)$$

where I_H is the drive current, n_{2D} the two-dimensional carrier concentration, μ the carrier mobility, $l(w)$ is the length(width) of the Hall voltage contacts and Δf the measurement bandwidth. Hence, for a given lead aspect ratio and Hall current, optimising the minimum detectable field requires minimising the carrier concentration and maximising the carrier mobility. Probes based on GaAs/$Al_xGa_{1-x}As$ heterostructures remain the material of choice for low temperature imaging but suffer from the undesirable degradation of their carrier mobility at room temperature [9]. This problem is less pronounced in narrow gap semiconductors and very good 300K figures-of-merit have been reported for a 0.5μm Hall cross device fabricated in a 320nm thick InSb film, albeit with little scope for further reduction in size [10]. Moreover, high-quality epitaxial growth of InSb-based probes is challenging and active layers are typically buried ≥50nm below the epilayer surface setting a fundamental lower bound on the spatial resolution.

In contrast, the very low, tunable carrier density of graphene as well as its unique band structure that gives rise to extremely high room temperature mobilities, make it an ideal material for nanoscale

Hall sensors [7]. In addition graphene is atomically thin, allowing the active sensor to be positioned extremely close to the sample surface for mapping with very high spatial resolution. Hall probes fabricated from exfoliated graphene [11], graphene grown on SiC [12] and chemical vapour deposited (CVD) graphene [13-17] have been extensively studied in the last decade and nanoscale CVD graphene sensors based on the intersection of 85nm wires with B_{min}~ 0.59G/Hz$^{0.5}$ were recently reported [18]. The carrier mobility of these devices was mainly limited by scattering from charge centres in the adjacent SiO_2 substrate layer and it has been demonstrated that the suspension of graphene above the surface [19] or the two-sided encapsulation with layers of hexagonal boron nitride (hBN) [20] can dramatically enhance the mobility with values as high as 10m^2/Vs demonstrated in encapsulated devices at room temperature. Encapsulation of micrometer-sized Hall sensors has also been shown to substantially reduce extrinsic doping effects [21] and 300K minimum detectable fields as low as B_{min} = 7mG/Hz$^{0.5}$ have been demonstrated for a 1μm Hall cross at a measurement frequency of 1kHz [22]. However, the fabrication of fully encapsulated sensors on a platform suitable for scanning probe microscopy is challenging, requiring a large number of complex process steps including the formation of 'edge' contacts to etched graphene as well as the integration of a secondary height sensor. Although magnetic imaging with sensors based on patterned bare CVD graphene has been demonstrated by Sonusen *et al*. [17], there have been no reports of this with encapsulated graphene Hall sensors. Here we report the development of a relatively simple process to fabricate semi-encapsulated graphene Hall sensors built by dry transfer onto pre-patterned gold contacts. We demonstrate 1μm-sized Hall cross sensors with excellent room temperature sensitivity ($S_I = V_H/(I_H.B)$ ~ 700V/AT) and good minimum detectable fields (B_{min} = 0.54G/Hz$^{0.5}$) and illustrate their application in an imaging study of labyrinth magnetic domains in a ferrimagnetic yttrium iron garnet (YIG) film.

Our Hall devices were assembled in an ambient environment on pre-patterned Si/SiO_2 substrates by the dry transfer of exfoliated flakes of graphene and hBN. The starting chips contained sets of four outer contacts and an integrated scanning tunnelling microscopy (STM) tip connected to large bond pads, patterned in a Cr(5nm)/Au(200nm) metallisation layer by direct laser write lithography in optical photoresist and lift-off. A set of four Cr(5nm)/Au(150nm) inner contacts was subsequently patterned at the location of the active sensor by electron beam lithography (EBL) of thick Copolymer/PMMA bilayer resist and lift-off. These comprised two long and narrow (1μm) pads for the drive current and two large area (6μm×19μm) voltage pads to maximise the contact area for stable van der Waals bonding and minimise the series resistance and reduce the Johnson noise into the preamplifier. There was a 4μm gap between the ends of both the current and voltage leads which was subsequently bridged by a graphene/hBN bilayer flake that was transferred on top.

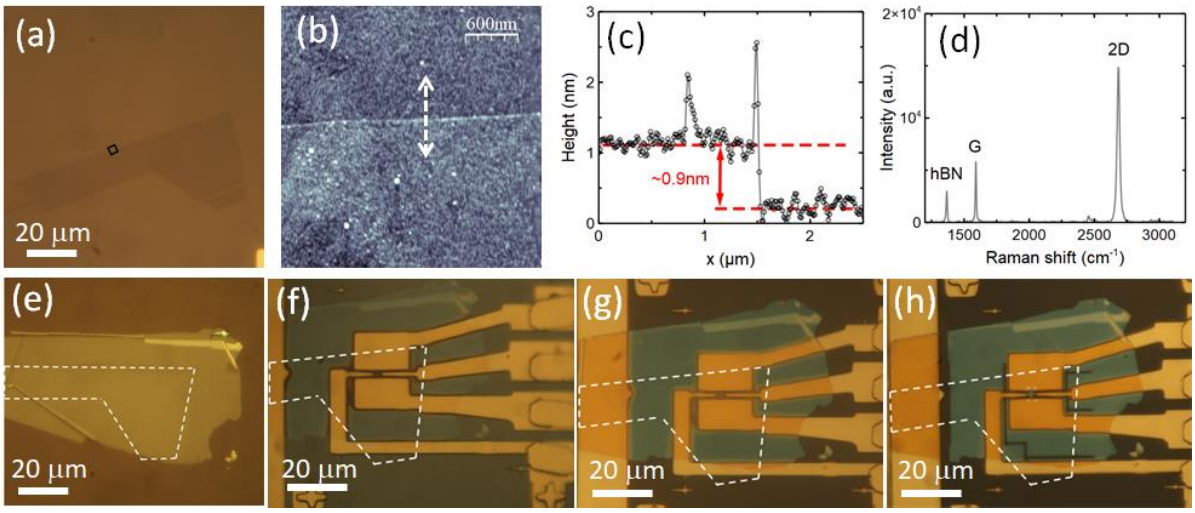

Figure 1. (a) Optical image of the monolayer graphene layer after exfoliation onto a Si/SiO_2 substrate. (b) AFM image captured at the edge of the graphene flake in the region shown by the black square in (a). (c) Topographic linescan along the indicated white dashed line in (b). (d) Raman spectrum of the monolayer graphene flake captured through the hBN encapsulation layer. (e) Optical image captured through the polymer stamp after hot pick-up of graphene with the hBN flake. The white dashed line indicates the footprint of the underlying graphene flake. (f) Optical image of the Hall sensor device after the graphene/hBN bilayer has been dropped onto the pre-patterned Au contacts with the delaminated PPC layer on top, and (g) after removal of the PPC in chloroform. (h) Completed device after ICP etching of trenches to define the Hall cross geometry sensor.

The active sensor layers were assembled using the "hot pick-up" technique developed by Pizzocchero *et al*. [23] whereby a polymer 'stamp' comprising a polydimethylsiloxane (PDMS) block coated with polypropylene carbonate (PPC) is employed to pick up a flake of hBN which is then used to manipulate a graphene flake that has been exfoliated onto an Si/SiO_2 substrate. Figs. 1(a)-(h) show details of a device at each stage of this process. Fig. 1(a) illustrates the graphene layer after exfoliation with Nitto tape onto Si/SiO_2, while Fig. 1(b) shows an atomic force microscope (AFM) image of the edge of the flake indicated by the black square in Fig. 1(a). A topographic line scan along the direction of the dashed black line is reproduced in Fig. 1(c) and the measured step height of 0.9 ± 0.05nm is consistent with a monolayer graphene flake on SiO_2 [24]. This assignment has been confirmed by performing Raman spectroscopy on the graphene flake through the hBN encapsulation layer at an excitation wavelength of 532nm and laser power of 250μW (Fig. 1(d)). The very narrow 2D peak at 2685 cm^{-1} whose intensity is about 2.5x higher than the G peak at 1590 cm^{-1} are established signatures of monolayer flakes [25]. Fig. 1(e) shows an optical image captured through the polymer stamp after hot pick-up of the graphene with the hBN flake. Fig. 1(f) shows the device after dropping the graphene/hBN bilayer onto the pre-patterned Au contacts with the delaminated PPC film on top, and

(g) after removal of PPC in chloroform. Finally Fig. 1(h) shows the completed device after definition of the Hall cross geometry by inductively coupled plasma (ICP) etching narrow 1μm wide trenches through a PMMA mask patterned by EBL using a SF_6/Ar gas mixture.

An expanded view of a completed Hall sensor is shown in Fig. 2(a) where the Hall current/voltage leads and STM tip have been labelled. The EBL design for the Hall cross was based on the intersection of two 1.0μm wide graphene leads. In practice we patterned eight sensors on a single 1cm square Si/SiO_2 substrate, which had been sectioned up with deep (1.4μm) ICP-etched trenches

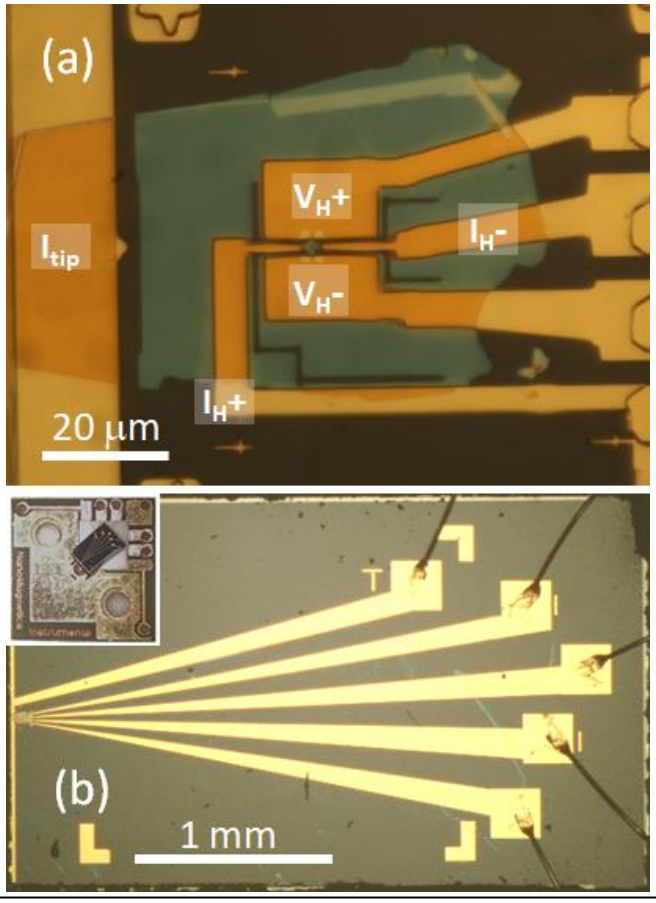

Figure 2. (a) Expanded view of the active area of the completed Hall sensor. The Hall current (I_H+/I_H-) and Hall voltage (V_H+/V_H-) leads and the STM tip (I_{tip}) have been indicated. (b) Optical image of the diced and wire bonded sensor chip. The inset shows the chip mounted on the 10mmx10mm package of the NanoMagnetics Instruments Ltd SHPM.

that were scored with a diamond scriber prior to contact deposition. This allowed the substrate to be readily cleaved into individual chips as the final step of the process. Fig. 2(b) shows one such chip after dicing which has been mounted on the 10mmx10mm sample puck of a commercial NanoMagnetics Instruments Ltd low temperature scanning Hall probe microscope and bonded with 25μm diameter gold wires. The inset to Fig. 2(b) illustrates the entire packaged device.

The packaged Hall sensor shown in Fig. 2 was screwed onto the end of the piezoelectric scanner tube of a NanoMagnetics Instruments Ltd low temperature SHPM equipped with a spring pin assembly for contacting the four Hall sensor leads and the STM tip. The two terminal lead resistances measured in air between pairs of Hall voltage and current contacts were 21.3kΩ and 21.5kΩ respectively. The Hall coefficient of the sensor was characterised at a current of 0.5μA using a calibrated bulk NdFeB magnet. The measured value of R_H=0.070±0.004Ω/G corresponds to a residual carrier concentration of 5.9±0.3×$10^{11}$$cm^{-2}$, yielding a lower bound for the carrier mobility in graphene of 375cm^2/Vs. Assuming that the thickness of our graphene monolayer is half the c-axis height of the unit cell of graphite (0.335nm) this corresponds to an effective 3D Hall coefficient of ~2.4×10^{-7} m^3/C. In practice we believe the two-lead resistances to be dominated by contact resistances at the graphene-gold contact interface and the true value of the mobility is expected to be considerably larger.

A ferrimagnetic yttrium iron garnet film with out-of-plane magnetic anisotropy was mounted on the sample puck of the inertial stick/slip approach mechanism, which hangs beneath the Hall sensor. The YIG film thickness was measured by reflectometry to be 9.20±0.05μm and had been coated with a 70nm conducting Au film to enable the STM feedback loop. The integrated STM tip metallisation at the very edge of the chip lies about 40μm away from the active Hall sensor and must be the first point to come into contact with the surface of the sample upon approach. The sample puck has three adjustable springs which allow one to precisely set a tilt angle of ~0.5° between the Hall probe and sample surface such that this condition is satisfied. The entire microscope head was placed in a vibration-isolated cryostat equipped with an electromagnet capable of providing in-plane fields up to ±750Oe. Prior to imaging measurements the sample space was pumped hard for two days (base pressure ~1.4×10^{-6}mbar) to remove water or any other volatile contaminants on the active sensor

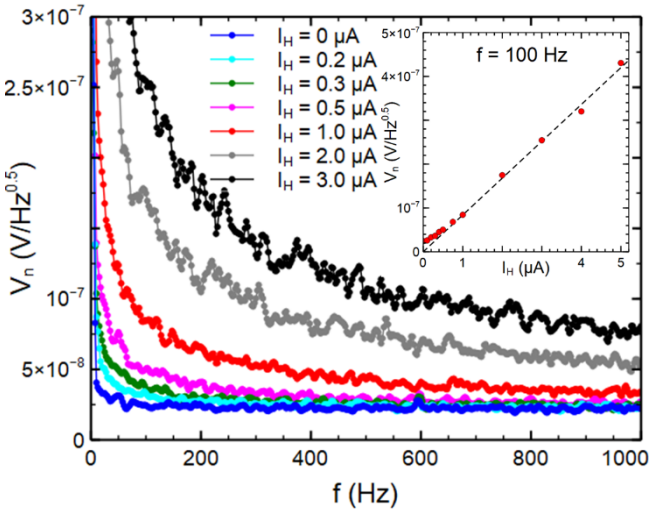

Figure. 3 Hall voltage noise per root bandwidth as a function of frequency for a range of different drive currents. The inset shows the noise per root bandwidth at a frequency of 100Hz plotted against the sensor drive current.

surface and then back-filled with an atmosphere of high purity He gas. Fig. 3 shows the frequency-dependence of the Hall voltage noise in the range 0-1000Hz at various drive currents, measured with an ultra-low noise preamplifier feeding a commercial spectrum analyser. Above a drive current of 0.5μA an abrupt increase in the low frequency noise is observed, with the 1/f noise corner shifting rapidly to higher frequencies at larger currents. At high frequencies the noise level approaches a floor of 23nV/Hz$^{0.5}$, in reasonable agreement with an estimate of the Johnson noise level based on the two-terminal resistances (19nV/Hz$^{0.5}$). The inset to Fig. 3 plots the noise voltage measured at 100Hz versus the drive current. The observed linear behaviour at high currents is in very good agreement with a conductivity fluctuation model proposed by Vandamme *et al*. [26] and discussed in detail for graphene Hall sensors in ref. [18]. In the Johnson noise limit at frequencies well above the 1/f noise corner with a 0.5μA drive current we estimate the minimum detectable field from equation (1) to be ~0.54G/Hz$^{0.5}$.

The sample was approached towards the Hall sensor until a tunnel current of 0.2nA was established at the STM tip within a feedback loop. The sample was then retracted about a hundred nanometres out of tunnel contact, allowing very rapid Hall probe scans of the local magnetic induction to be captured without height control and greatly reducing the risk of sensor damage due to a 'head crash'. The YIG sample exhibits labyrinth-like magnetic domains with a characteristic periodicity of ~14μm, composed of stripes with up or down magnetisation as shown in the polar magneto optical Kerr effect (MOKE) image of Fig. 4(a). Fig. 4(b) shows a single 128×128 pixel SHPM image of the domain structure captured at 300K in zero applied field. A dc Hall current of 0.5μA and a measurement bandwidth for the Hall voltage of 0.1kHz were used and each image was scanned at the fastest speed allowed by our microscope (~240s/image). Although the single scan images are perfectly acceptable, the low frequency noise can be effectively suppressed by averaging several successive images as illustrated by the much higher quality image of Fig. 4(c) achieved after averaging 16 frames. The apparent weak variation in resolution between the top and bottom of images is a result of the small tilt angle that has been set between the sample surface and scanner plane. As a consequence, the sample-sensor spacing is slightly larger at the bottom of the image than at the top, leading to a weak gradient in spatial resolution. In a second experiment successive domain images (Figs. 4(d)-(g)) were captured as the in-plane field (parallel to the arrow in Fig. 4(d)) was increased from zero to 715Oe and back to zero again. Although the YIG film exhibits out-of-plane anisotropy with nearly all moments perpendicular to this in-plane field, rotated moments at the centre of Bloch walls do still couple, leading to persistent changes in the magnetic domain topology (c.f., Figs. 4(d) and (g) which are both at H=0).

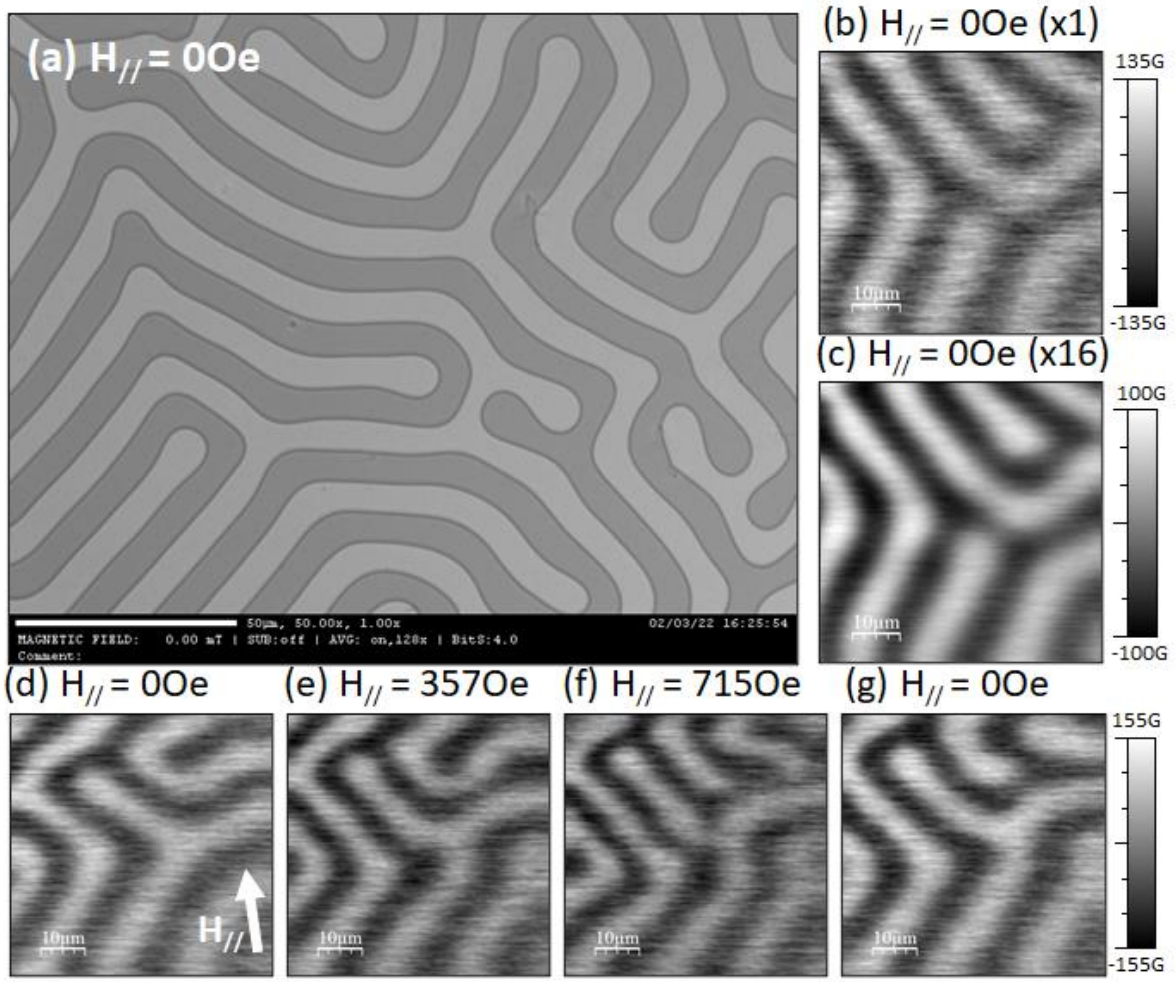

Figure. 4 Polar magneto optical Kerr effect (MOKE) image of the ferrimagnetic YIG film showing the characteristic labyrinth magnetic domain structure (scale marker is 50µm). (b) Single 128×128 pixel room temperature SHPM image of the domain structure captured at H=0, I_H=0.5µA and a measurement bandwidth ∆f=0.1kHz. The image was scanned at approximately one line every 2s. (c) Higher quality image achieved after averaging 16 consecutive frames. (d)-(g) domain images captured after the in-plane field (parallel to the arrow in (d)) was increased from zero to 715Oe and back to zero again. All four images have been constructed with the same colour scale indicated by the colourbar on the right hand side. Comparison of (d) and (g), which are both at H=0, reveals

There remains considerable scope for improving the figures-of-merit of these sensors still further. The estimated minimum detectable field of ~0.54G/Hz$^{0.5}$ in our 1µm device at 300K is in reasonable agreement with the results for similar sized unencapsulated CVD graphene sensors in ref [18] which had been tuned with a back gate to much lower carrier concentrations. It is well established that the carrier mobility in graphene shows quite a strong inverse dependence on the carrier density [27] and the optimum minimum detectable fields are obtained just either side of the charge neutrality point (CNP) [18]. We estimate that B_{min} could be lowered by at least a factor of 2 if the carrier density

was reduced towards the CNP, e.g., by using the conducting n^+-Si substrate as a back gate. Changes could also be made to the fabrication process to reduce extrinsic sources of disorder. The contact resistance is known to be a strong function of the contact metal and its morphology, and alternative contact metals (e.g., Nickel) and different physical deposition methods (e.g., evaporation, sputtering) should be explored to minimise these [28]. The hot pick-up transfer system could also be moved to an inert glovebox environment to prevent the contamination of devices with water and other volatile species during assembly.

The current 1μm size of Hall probes could still be greatly reduced to improve the achievable spatial resolution. Since the hBN encapsulation layer is only ~20nm thick it should be possible to use EBL and ICP etching to pattern Hall crosses based on ≤50nm wirewidths, provided devices are carefully annealed to remove mechanical strain in the graphene/hBN bilayer after transfer. An elegant solution would be to pattern the Hall cross in the exfoliated graphene layer before hot pick-up with the hBN flake so that no further processing would be required after transfer onto the pre-patterned contacts. This approach would also allow the flakes to be suspended above the substrate on thick inner contact pads, substantially eliminating scattering from charge centres in the SiO_2 layer below, increasing the carrier mobility and reducing the Johnson noise. Alternatively the contacts could be pre-patterned in a thick hBN flake that is transferred immediately after definition of the outer contacts. This would allow a fully encapsulated sensor to be realised which should lead to a dramatic increase in the carrier mobility and a reduction in the minimum detectable field closer to the value of $7mG/Hz^{0.5}$ reported in ref. [22]. Finally, our Hall probe design could easily be incorporated into a 'plug and play' sensor option for most commercial atomic force microscopes, making it very easy for new users to adopt the technology.

In conclusion, we report the development of a relatively simple process to fabricate semi-encapsulated graphene Hall sensors built by dry transfer onto pre-patterned gold contacts. We have characterised 1μm-sized Hall cross sensors of this type which exhibit excellent room temperature sensitivity (S_I ~ 700V/AT) and good minimum detectable fields (B_{min} = $0.54G/Hz^{0.5}$). We illustrate the application of these sensors in an SHPM imaging study of labyrinth magnetic domains in a ferrimagnetic yttrium iron garnet film. There is considerable scope for improving the figures-of-merit of our sensors and various possible future developments are discussed.

The supplementary material contains a schematic diagram that details the steps used to assemble the heterostructure Hall sensor along with side views of the layers making up the device.

P.L., D.C. and S.J.B. acknowledge financial support from EPSRC in the UK under grant number EP/R007160/1 and the Nanocohybri COST Action CA-16218. D.C. was also supported by a PhD studentship from Lloyds Register Foundation ICON (award nos. G0086). Z.J.L. and S.D. acknowledge

support from the Royal Society under University Research Fellowship UF160272. P.S. acknowledges the support of the Henry Royce Institute under grant number EP/R00661X/1. We also acknowledge access to the University of Bath Nanofabrication Facility where device fabrication has been performed as well as training and process support from Dr Stephen Wedge and Dr Siva Sivaraya. In addition we acknowledge access to the Material and Chemical Characterisation Facility (MC^2) at the University of Bath (doi.org/10.15125/mx6j-3r54) where Raman spectroscopy was performed.

AUTHOR DECLARATIONS

Conflict of Interest

The authors have no conflicts to disclose.

DATA AVAILABILITY

The data that support the findings of this study are openly available in the University of Bath Research Data Archive at **https://doi.org/10.15125/BATH-XXXXX**.

REFERENCES

[1] Y. Martin, and H. K. Wickramasinghe, Appl. Phys. Lett. **50**, 1455 (1987).

[2] J. J. Sáenz, N. García, P. Grütter, E. Meyer, H. Heinzelmann, R. Wiesendanger, L. Rosenthaler, H. R. Hidber, and H-J Güntherodt, J. Appl. Phys. **62**, 4293 (1987).

[3] D. Mitin, M. Grobis, and M. Albrecht, Rev. Sci. Instrum. **87**, 023703 (2016).

[4] A. M. Chang, H. D. Hallen, L. Harriot, H. F. Hess, H. L. Loa, J. Kao, R. E. Miller, and T. Y. Chang, Appl. Phys. Lett. **61**, 1974 (1992).

[5] A. Oral, S. J. Bending, and M. Henini, Appl. Phys. Lett. **69**, 1324 (1996).

[6] Gopalakrishnan Balasubramanian, I. Y. Chan, Roman Kolesov, Mohannad Al-Hmoud, Julia Tisler, Chang Shin, Changdong Kim, Aleksander Wojcik, Philip R. Hemmer, Anke Krueger, Tobias Hanke, Alfred Leitenstorfer, Rudolf Bratschitsch, Fedor Jelezko, and Jörg Wrachtrup, Nature **455**, 648 (2008).

[7] David Collomb, Penglei Li, and Simon Bending, J. Phys. Condens. Matter **33,** 243002 (2021).

[8] Adarsh Sandhu, Kouichi Kurosawa, Munir Dede, and Ahmet Oral, Jpn. J. Appl. Phys. **43,** 777 (2004).

[9] K. Vervaeke, E. Simoen, H. Borghs, V. V. Moshchalkov, Rev. Sci. Instrum. **80**, 074701 (2009).

[10] A. Sandhu, H. Sanbonsugi, I. Shibasaki, M. Abe, andH. Handa, Jpn. J. Appl. Phys. **43**, 868 (2004).

[11] K. S. Novoselov, Z. Jiang, Y. Zhang, S. V. Morozov, H. L. Stormer, U. Zeitler, J. C. Maan, G. S. Boebinger, P. Kim, and A. K. Geim, Science **315**, 1379 (2007).

[12] V. Panchal, K. Cedergren, R. Yakimova, A. Tzalenchuk, S. Kubatkin, and O. Kazakova, J. Appl. Phys. **111**, 07E509 (2012).

[13] C. C. Tang, M. Y. Li, L. J. Li, C. C. Chi, and J. C. Chen, Appl. Phys. Lett. **99**, 112107 (2011).

[14] Huilong Xu, Zhiyong Zhang, Runbo Shi, Honggang Liu, Zhenxing Wang, Sheng Wang, and Lian-Mao Peng, Scientific Reports **3**, 1207 (2013).

[15] Huilong Xu, Le Huang, Zhiyong Zhang, Bingyan Chen, Hua Zhong, and Lian-Mao Peng, Appl. Phys. Lett. **103**, 112405 (2013).

[16] Le Huang, Zhiyong Zhang, Bingyan Chen, Xiaomeng Ma, Hua Zhong, and Lian-Mao Peng, Appl. Phys. Lett. **104**, 183106 (2014).

[17] S. Sonusen, O. Karci, M. Dede, S. Aksoy, and A. Oral, Appl. Surf. Sci. **308**, 414 (2014).

[18] David Collomb, Penglei Li, and Simon Bending, Scientific Reports **9**, 14424 (2019).

[19] Xu Du, Ivan Skachko, Anthony Barker, and Eva Y. Andrei, Nature Nanotech. **3**, 491 (2008); K. I. Bolotin, K. J. Sikes, Z. Jiang, M. Klima, G. Fudenberg, J. Hone, P. Kim, and H. L. Stormer, Solid State Commun. **146**, 351 (2008).

[20] Alexander S. Mayorov, Roman V. Gorbachev, Sergey V. Morozov, Liam Britnell, Rashid Jalil, Leonid A. Ponomarenko, Peter Blake, Kostya S. Novoselov, Kenji Watanabe, Takashi Taniguchi, and A. K. Geim, Nano Lett. **11**, 2396 (2011).

[21] Jan Dauber, Abhay A. Sagade, Martin Oellers, Kenji Watanabe, Takashi Taniguchi, Daniel Neumaier, and Christoph Stampfer, Appl. Phys. Lett. **106**, 193501 (2015).

[22] Brian T. Schaefer, Lei Wang, Alexander Jarjour, Kenji Watanabe, Takashi Taniguchi, Paul L. McEuen, and Katja C. Nowack, Nat. Commun. **11**, 4163 (2020).

[23] Filippo Pizzocchero, Lene Gammelgaard, Bjarke S. Jessen, José M. Caridad, Lei Wang, James Hone, Peter Bøggild, and Timothy J. Booth, Nat. Commun. **7**, 11894 (2016).

[24] Cameron J Shearer, Ashley D Slattery, Andrew J Stapleton, Joseph G Shapter, and Christopher T Gibson, Nanotechnology **27,** 125704 (2016).

[25] A. C. Ferrari, J. C. Meyer, V. Scardaci, C. Casiraghi, M. Lazzeri, F. Mauri, S. Piscanec, D. Jiang, K. S. Novoselov, S. Roth, and A. K. Geim, Phys. Rev. Lett. **97,** 187401 (2006).

[26] L. K. J. Vandamme, and A. H. De Kuijper, Solid-State Electron. **22**, 981 (1979).

[27] E. Zion, A. Butenko, A. Sharoni, M. Kaveh, and I. Shlimak, Phys. Rev. B **96**, 245143 (2017).

[28] Teresa Cusati, Gianluca Fiori, Amit Gahoi, Vikram Passi, Max C. Lemme, Alessandro Fortunelli, and Giuseppe Iannaccone, Scientific Reports **7**, 5109 (2017).